energies

MDPI

Article

Computational Modeling of Gurney Flaps and Microtabs by POD Method

Unai Fernandez-Gamiz [1,*], Macarena Gomez-Mármol [2] and Tomas Chacón-Rebollo [2,3]

1 Nuclear Engineering and Fluid Mechanics Department, University Basque Country, UPV/EHU, 01006 Vitoria, Spain
2 Department Ecuac Diferenciales & Anal Numer, Fac Mathematics, University Seville, 41012 Seville, Spain; macarena@us.es
3 Instituto de Matemáticas Universidad de Sevilla (IMUS), University Seville, 41012 Seville, Spain; chacon@us.es
* Correspondence: unai.fernandez@ehu.eus; Tel.: +34-945014066

Received: 6 July 2018; Accepted: 10 August 2018; Published: 11 August 2018

Abstract: Gurney flaps (GFs) and microtabs (MTs) are two of the most frequently used passive flow control devices on wind turbines. They are small tabs situated close to the airfoil trailing edge and normal to the surface. A study to find the most favorable dimension and position to improve the aerodynamic performance of an airfoil is presented herein. Firstly, a parametric study of a GF on a S810 airfoil and an MT on a DU91(2)250 airfoil was carried out. To that end, 2D computational fluid dynamic simulations were performed at Re = 10^6 based on the airfoil chord length and using RANS equations. The GF and MT design parameters resulting from the computational fluid dynamics (CFD) simulations allowed the sizing of these passive flow control devices based on the airfoil's aerodynamic performance. In both types of flow control devices, the results showed an increase in the lift-to-drag ratio for all angles of attack studied in the current work. Secondly, from the data obtained by means of CFD simulations, a regular function using the proper orthogonal decomposition (POD) was used to build a reduced order method. In both flow control cases (GFs and MTs), the recursive POD method was able to accurately and very quickly reproduce the computational results with very low computational cost.

Keywords: wind energy; flow control; Gurney flaps; microtabs; proper orthogonal decomposition; reduced order method

1. Introduction

The significant increase of wind turbine size and weight in the past decade has made it impossible to control them as they were 30 years ago. Wind turbine rotors of 140 m or even more are now a reality. Johnson et al. [1] compiled some of the most important load control techniques that can be used in wind turbines to ensure a safe and optimal operation under a diversity of atmospheric environments. These include blades made of soft, flexible materials that change shape in response to wind speed or aerodynamic loads, aerodynamically-shaped rotating towers, flexible rotor systems with hinged blades, and other advanced control systems. The larger the size of a wind turbine, the higher the structural and fatigue loads, which affect the rotor and other key mechanisms of the turbine. A reduction of these severe loads can be achieved by developing novel load control techniques. Loads on wind turbines are normally divided into extreme structural loads and fatigue loads. Reducing these fatigue loads is a main goal, which can reduce the maintenance costs and improve the reliability of wind turbines (see Baek et al. [2]).

Several flow control systems were developed in the past decades. Most of them were created for aeronautical issues, and this was their first research field and application. Researchers are currently working to optimize and introduce this type of device in wind turbines [3]. Wood [4] developed a four-layer scheme that allows classification of the diverse concepts. As explained in Aramendia et al. [5,6], they can be classified as actives or passives devices depending on their operating principle. To alleviate loads successfully, it is indispensable that the device to be able to reduce the generated lift. The studies presented by Johnson et al. [7] and Frederick et al. [8] provide different ways of using this type of device to mitigate turbine loads.

Gurney flaps (GFs) were originally used for lift enhancement in the field of aeronautics [9,10]. The advantages and limitations of these devices have been acutely documented [9,11]. The first application was in racing cars, as small vertical strips attached to the trailing edge (TE) of the wing. The GF was first considered by Liebeck [12] and improved by Jeffrey et al. [13,14]. Tang and Dowell [15] compared the experimental loading of a NACA 0012 airfoil with both static and oscillating trailing-edge GFs using an incompressible Navier–Stokes solver. A movable GF on a NACA 4412 airfoil was studied by Camocardi et al. [16], where the flow pattern behavior in the near wake of the airfoil was investigated. Lee [17] also studied the impact of GFs of different sizes and perforations on the growth and development of the tip vortex generated by a NACA 0012 airfoil using particle image velocimetry (PIV). Recently, Cole et al. [18] studied the effect of GFs of different heights, and the results indicated that the airfoil shape is decisive in the aerodynamic performance of the airfoil with GFs. Recently, researchers have returned to GFs to study prospective benefits in rotorcrafts and helicopters applications [13–15]. Liu et al. [19] and Min et al. [20] used microflaps for vibration reduction in helicopter rotors. Additionally, the influence of GFs on the power output performance of a 5 MW horizontal axis wind turbine was investigated by Fernandez-Gamiz et al. [21]. Increments in the average power output of 10.4% and 3.5% were found at two different wind velocity realizations. GFs appear to be one of most appropriate devices to improve reliability and/or power output in large wind turbines.

Microtabs (MTs) are defined as small tabs situated near the trailing edge (TE) of an airfoil, and project perpendicular to the surface of the airfoil by a few percent of the chord length (1–2% of c) corresponding to the boundary layer thickness. These MTs jet the flow in the boundary layer away from the airfoil surface, bringing a recirculation zone at the rear of the tab and affecting the aerodynamic behavior, moving the flow separation zone and consequently changing the lift. The lift can be enhanced by deploying the MT on the pressure side of the airfoil; on the contrary the lift is reduced if the MT is deployed on the suction side. MT concept and flow around a trailing-edge region during tab pressure-side deployment can be found in Chow et al. [22]. Van Dam [23] carried out multiple studies and investigations into this topic, including computational fluid dynamics (CFD) simulations and wind tunnel experiments, in order to determine their optimal distribution height and location. As in previous studies, the results provided that the best place to situate the lower surface tab with respect to lift and drag was around 0.95 c with a height of 0.01 c and around 0.90 c for the upper surface tab. MTs present some attractive features for wind turbine control applications, such as small size, design simplicity, and low set-up cost [24]. They can also be installed without significant changes in the actual techniques to manufacture the profiles. Tsai et al. [25] recently presented an innovative design to improve the MT performance. This new MT system is based on a four-bar linkage, providing an increase of the maximum tab height in relation to the existing MT system and better stability due to the four-bar linkage mechanism. Furthermore, blade element momentum (BEM)-based computations were performed in the study of Fernandez-Gamiz et al. [26] to investigate the effect of the MTs on the National Renewable Energy Laboratory (NREL) 5 MW wind turbine power output with different wind speed realizations. The results showed a considerable increase in the average wind turbine power due to the implementation of the MTs. In the academia–industry joint study of Hwangbo et al. [27], two different methods were developed to estimate and quantify the effect of some passive flow control devices on a multi-megawatt wind turbine power production. Lee et al. [28] also presented an

innovative kernel plus method to quantify a turbine's upgrade. A directory of generalizable methods to investigate wind turbine power curve upgrades in real environments through operational data was presented in Astolfi et al. [29].

Model reduction methods are now basic numerical tools in the treatment of large-scale parametric problems appearing in real-world problems (see Azaïez et al. [30,31] and references therein, Pinnau et al. [32]). They are applied with success, for instance, in signal processing, the analysis of random data, in the solution of parametric partial differential equations and control problems, among others. In signal processing, Karhunen–Loève expansion (KLE) provides a reliable procedure for a low-dimensional representation of spatiotemporal signals. Different research communities use different terminologies for the KLE. It is named singular value decomposition (SVD) in linear algebra, principal components analysis (PCA) in statistics and data analysis, and is referred to as proper orthogonal decomposition (POD) in mechanical computation. These techniques allow a large reduction of computational costs, thus making affordable the solution of many parametric problems of practical interest, which would otherwise be out of reach. From a mathematical point of view, all three techniques fit into a common theoretical framework, provided by the KLE expansion. We will use the name "POD", as we are within the framework of mechanical computation. In this paper, apply POD to the analysis of the behavior of passive flow control devices on wind turbines.

As previously described, we made different simulations by means of CFD methods in which we computed the lift-to-drag ratio for several angles of attack and geometrical design parameters of GF and MTs. Following this procedure, we constructed a POD approximation of the function that transforms the geometrical design parameters of either GFs or MTs (understood as independent variables in mathematical terms) on the lift-to-drag ratio (understood as a dependent variable). This function will allow computation of the lift-to-drag ratio for any values of the independent variables, in particular those out from the computational grid. This computation can be carried out very quickly, as it does not need to use CFD simulations. However the usual POD analysis only applies to functions that transform a single independent variable in a dependent variable. Instead, we use an extension of POD to multi-parametric functions, called recursive POD. The mathematical development of this method as well as some applications can be found in References [30–33]. Its application to the computation of lift-to-drag ratios considered here is described in detail in Section 3.

The purpose of constructing the considered POD approximation was to validate its application to accurately computing the lift-to-drag ratio, and more specifically its maximum, in view of some possible applications of interest. For instance, it could easily be implemented to take advantage of active flow control strategies, which agrees with the study of Yen et al. [34], which presented MTs as high-potential devices for active load control.

The paper is structured as follows: In Section 2 we state the numerical setup for the computation of the lift-to-drag ratio of the GFs and MTs considered. In Section 3 we describe the Recursive POD method and its application to the computation of lift-to-drag ratios. Section 4 is devoted to presenting the results (both the CFD computations and the validation of the POD approximation), and finally Section 5 presents some relevant conclusions.

2. Numerical Setup

2.1. Gurney Flap Lay-Out

An S810 airfoil model developed by NREL was selected for the GF parametric study and the data was extracted from the report of Reuss-Ramsay et al. [35], where the airfoil was tested on a subsonic wind tunnel under steady state conditions. The range of the airfoil angle of attack was defined as from -4 to 10 degrees. Figure 1 illustrates the geometry with the current settings consisting of a S810 airfoil with a Gurney flap in the airfoil trailing edge. y represents the GF size and c the airfoil chord length.

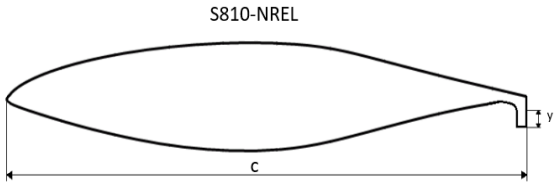

Figure 1. S810 National Renewable Energy Laboratory (NREL) aerodynamic airfoil and Gurney flap (GF) dimension.

Dimension y represents the height of the GF in percentage of c. Twelve cases were analyzed depending on the distance measured respective to the airfoil chord length (see Table 1).

Table 1. Case names and GF dimensions.

Id	Case Name	y (% of c)
0	S810	no GF
1	S810GF025	0.25
2	S810GF050	0.50
3	S810GF075	0.75
4	S810GF100	1.00
5	S810GF125	1.25
6	S810GF150	1.50
7	S810GF175	1.75
8	S810GF200	2.00
9	S810GF225	2.25
10	S810GF250	2.50
11	S810GF275	2.75
12	S810GF300	3.00

The numerical solution was performed applying Reynolds Averaged Navier–Stokes (RANS) equations for steady state flow in the open source CFD code OpenFOAM (Version 2.4.0, The OpenFOAM Foundation Ltd., London, UK) [36]. The SIMPLE algorithm has been used for the coupling of pressure–velocity and a second-order linear-upwind scheme for the discretization of the convective terms. The k-ω Shear Stress Transport (SST) turbulence model of Menter [37] has been used for these computations due to its higher performance in separated flows, as reported by Kral [38] and Gatski [39]. This model is a blend of the well known Wilcox's k-ω model and the k-ε model. RANS based simulations with the SST turbulence model for different configurations are presented in the study of Mayda et al. [40] for airfoil applications. The Reynold number is Re = 10^6 based on the airfoil chord length of c = 1 m. The grid of the computations consists of 155,000 structured cells, with the first cell height $\Delta z/c$ of 1.45 × 10^{-6}, where c is the airfoil chord length. The stretching factor in the chord-wise and normal directions is made by double-sided *tanh* functions based on Thompson et al. [41] and Vinokur [42]. The numerical domain was determined to have a wall y + less than 1 over the surface of the airfoil. The domain was designed with a radius of 32 times the airfoil chord length, according to the recommendations of Sørensen et al. [43]. The dimensions of the computational domain normalized with the airfoil chord length are shown in Figure 2.

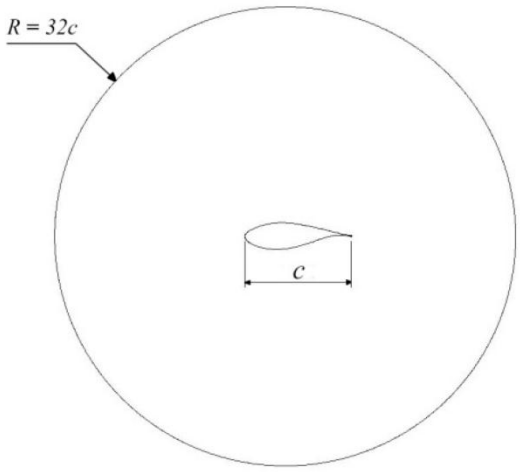

Figure 2. Computational domain size (not to scale).

Figure 3 illustrates the results of the CFD simulations alongside the experimental results extracted from [35] for all angles of attack of the airfoil. The CFD results followed the tendency of experimental ones reasonably well. Equations (1) and (2) were used to determine the lift and drag coefficients, respectively:

$$C_L = \frac{F_L}{\frac{1}{2}\rho U_\infty^2 c} \quad (1)$$

$$C_D = \frac{F_D}{\frac{1}{2}\rho U_\infty^2 c} \quad (2)$$

The air density was defined as $\rho = 1.204\ kg/m^3$ and the free stream velocity far ahead of the airfoil was $U_\infty = 56.48\ m/s$. Since the computations have been carried out in two dimensions, F_L and F_D are the lift and drag forces per unit of area. A dependency study of the mesh was carried out to prove adequate grid resolution. Therefore, the Richardson extrapolation method was applied to the lift-to-drag ratio calculations in the clean airfoil S810 without any device implemented. Figure 3 represents the assessment between the experiments and the results of the CFD computatons with three different meshes: 38,750 (coarse), 75,500 (medium), and 155,000 (fine) cells.

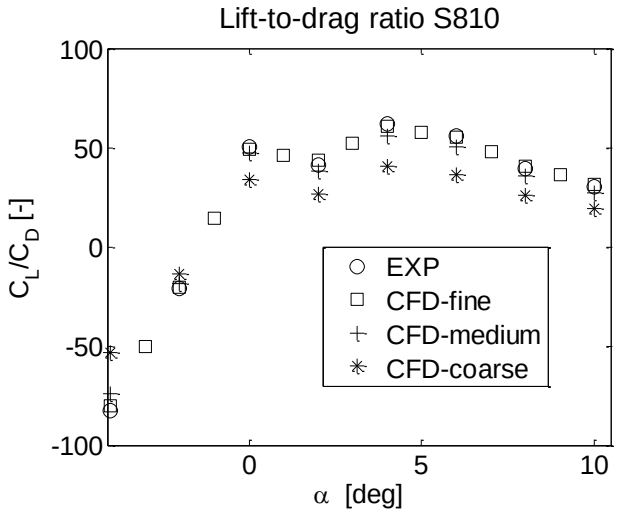

Figure 3. Lift-to-drag ratio of the numerical simulations versus experimental data of the clean airfoil s810 without any flow control device. CFD: computational fluid dynamics.

The results of the mesh dependency study is shown in Table 2. RE represents the solution of the Richardson extrapolation, R the ratio of errors, and p the order of accuracy. Since the value of R was less than 1, all integral quantities converged monotonically for all angles of attack. As illustrated in Figure 3, the numerical results obtained with the fine mesh predicted the experimental lift-to-drag ratios well. Therefore, this higher resolution mesh was used for the current computations.

Table 2. Results of the mesh independency study. AoA: angle of attack.

AoA	Mesh			Richardson Extrapolation		
	Coarse	Medium	Fine	RE	p	R
−4	−53.53	−77.00	−82.35	−80.77	2.13	0.23
−2	−13.65	−19.53	−21.00	−20.51	2.00	0.25
0	34.14	47.19	50.20	49.30	2.12	0.23
2	26.63	38.10	40.96	40.16	2.19	0.22
4	40.37	57.14	62.11	60.01	1.75	0.30
6	36.21	50.14	55.71	52.00	1.32	0.40
8	25.70	36.97	39.53	38.78	2.13	0.23
10	19.44	27.66	29.90	29.06	1.87	0.27

2.2. Microtab Layout

The airfoil chosen for the parametric study of the MT was the well-known DU91W(2)250 presented in Timmer et al. [44] and widely used by wind turbine blade manufacturers. The MT size and position in the airfoil is sketched in Figure 4. The dimension Y represents the size of the MT and X the position from the leading edge (LE).

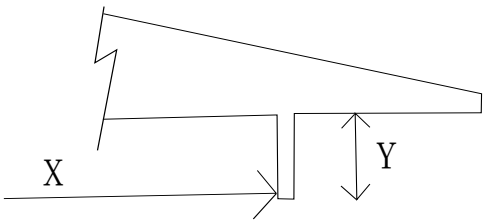

Figure 4. Location of the microtab (MT) from the airfoil leading edge X and size of the MT denoted as Y.

Twelve cases were determined depending on the distance measured from the leading edge (LE) as percent of the airfoil chord length c. These cases were: 0.93 c, 0.94 c, 0.95 c, and 0.96 c. The MT size relative to the chord length measured in percentage was 0.01 c, 0.015 c, and 0.02 c. To have an idea of the real size of the MT, the chord length of the DU91W(2)250 airfoil in the NREL 5 MW wind turbine developed by Jonkman et al. [45] is around 4 m, thus the size of the MTs varied between 0.04 and 0.08 m.

The MTs were positioned on the airfoil pressure surface and were investigated for ten angles of attack, from 0° to 9°. Table 3 illustrates the combination of all MT locations, giving 120 different cases to study. This is based on the cases presented in Fernandez-Gamiz et al. [26], but at a Reynolds number of Re = 10^6. The clean airfoil DU91W(2)250 without any device implemented was also simulated to investigate the effects of all the MTs described in Table 3.

Table 3. MT cases and denominations.

Case	x (% c)	y (% c)	Case Name
1	No MT	No MT	DU91W(2)250
2	93	1.0	DU91W2250MT9310
3	93	1.5	DU91W2250MT9315
4	93	2.0	DU91W2250MT9320
5	94	1.0	DU91W2250MT9410
6	94	1.5	DU91W2250MT9415
7	94	2.0	DU91W2250MT9420
8	95	1.0	DU91W2250MT9510
9	95	1.5	DU91W2250MT9515
10	95	2.0	DU91W2250MT9520
11	96	1.0	DU91W2250MT9610
12	96	1.5	DU91W2250MT9615
13	96	2.0	DU91W2250MT9620

3. POD Method

The POD method basically consists of the representation of data with a space of very low dimension. This method was initially proposed by Lumley in 1970 in the context of turbulence. The base of functions that comprise the method has low dimension, and by its characteristics it is possible to reconstruct an approximation of the solution of the model with a considerable reduction of computational resources.

The POD method objectively extracts the optimal base patterns of parametric functions from the experimental data to describe the characteristics of that data set. The set of basic functions (commonly named "POD modes") is optimal insofar as that finite number of functions captures most of the information or gives the best representation of the system among all spaces of the same dimension. In mathematical terms, the "best representation" property means that the mean quadratic error (with respect to the parameter) between the function to be approximated and the approximation provided by the POD space is the smallest possible among all spaces of the same dimension.

On the other hand the POD method has some difficulties in determining the basic functions when the data are very large in quantity. To solve this problem, Sirovich in 1987 proposed the method of snapshots, which consists of using as data the values of the function to be approximated, computed for a set of parameters located in a grid. Based on the snapshots, the set of orthogonal functions that capture most of the information is obtained, whenever the parameter grid is small enough. In the case of microtabs, the function we want to approximate is the lift-to-drag ratio, which depends on three parameters, as described in Section 2.2: the angle of attack α, the location of the MT from the airfoil leading edge represented by X, and the device height Y. In the present study, since we have three parameters to determine the basic functions, we applied the POD method recursively. To describe the recursive POD approximation to this function f, assume that the parameters α, x, and y respectively vary in intervals $A = [a_1, a_2]$, $X = [b_1, b_2]$, and $Y = [c_1, c_2]$. Denote by $L^2(\Omega)$ the family of functions of integrable square defined in a set Ω. The Karhunen–Loève theory ensures that f admits a representation of the form.

$$f(\alpha, x, y) = \sum_{m \geq 0} \sigma_m \varphi_m(x, y) v_m(\alpha), \tag{3}$$

where the series is convergent in $L^2(A \times X \times Y)$ and the sets of modes $(v_m)_{m \geq 0}$ and $(\varphi_m)_{m \geq 0}$ are respectively orthonormal in $L^2(A)$ and in $L^2(X \times Y)$. Moreover, the singular values σ_m are non-negative and converge to zero.

We next applied the POD expansion to each mode $\varphi_m(x,y)$. There are two sets of modes $\left(u_k^{(m)}\right)_{k\geq 0}$ and $\left(w_k^{(m)}\right)_{k\geq 0}$ which are respectively orthonormal in $L^2(X)$ and $L^2(Y)$, such that φ_m admits the representation:

$$\varphi_m(x,y) = \sum_{k\geq 0} \sigma_k^{(m)} u_k^{(m)}(x) w_k^{(m)}(y), \tag{4}$$

where the expansion is convergent in $L^2(X\times Y)$. Additionally, the singular values $\left(\sigma_k^{(m)}\right)_{k\geq 0}$ are non-negative and decrease to zero. Then, the function f admits the expansion:

$$f(\alpha,x,y) = \sum_{m\geq 0}\sum_{k\geq 0} \sigma_m \sigma_k^{(m)} v_m(\alpha) u_k^{(m)}(x) w_k^{(m)}(y), \tag{5}$$

where the sum is convergent in $L^2(A\times X\times Y)$. The feasible recursive POD approximation of the function f consists of truncating the series (3) and (5) to a finite number of summands (e.g., M and K). Further, as the function f can be computed only for some values of $\alpha:\ \alpha_1,\ldots,\alpha_N$, $x=x_1,\ldots,x_P$, and $y=y_1,\ldots,y_Q$, the recursive POD in principle provides an approximation of f at these values:

$$f(\alpha_i,x_j,y_l) = \sum_{m=0}^{M}\sum_{k=0}^{K} \sigma_m \sigma_k^{(m)} v_m(\alpha_i) u_k^{(m)}(x_j) w_k^{(m)}(y_l). \tag{6}$$

Then, a fast 1D interpolation procedure (e.g., by spline functions) is used to compute $f(\alpha,x,y)$ for different values of (α,x,y) in $A\times X\times Y$. The source of errors in the recursive POD approximation is not only the truncation of series (6), but also this interpolation procedure. Then, the interpolation grid size should be small enough to ensure good error levels. Note that the interpolation grid is actually the parameter grid for which the values $f(\alpha_i,x_j,y_l)$ are computed, and a decrease in grid size leads to a larger number of CFD computations.

The computation of the POD expansion for bi-variate functions (e.g., for function φ_m at regularly spaced grid nodes $x = x_1,\ldots,x_P$ and $y = y_1,\ldots,y_Q$) is as follows: The vectors $U_k = \left[u_k^{(m)}(x_1),\ \ldots,\ u_k^{(m)}(x_P)\right]$ and $W_k = \left[w_k^{(m)}(y_1),\ \ldots,\ w_k^{(m)}(y_Q)\right]$ respectively are the $K \leq \min\{P,Q\}$ first right and left eigenvectors of the singular value decomposition of the matrix:

$$X^{(m)} = \begin{pmatrix} \varphi^{(m)}(x_1,y_1) & \cdots & \varphi^{(m)}(x_P,y_1) \\ \vdots & \ddots & \vdots \\ \varphi^{(m)}(x_1,y_Q) & \cdots & \varphi^{(m)}(x_P,y_Q) \end{pmatrix}$$

while the coefficients $\sigma_k^{(m)}$, $k=1,\ldots,K$ are the corresponding singular values.

Figure 5 illustrates the error that is committed in the method for different norms to approximate a smooth function of two variables, reported in Azaïez et al. [31]. On the x-axis we have the total number of modes M, and on the y-axis we have the error that is committed in logarithmic coordinates. We can observe that very few modes provided an excellent approximation of our function. The results presented in Section 4 were achieved with seven modes.

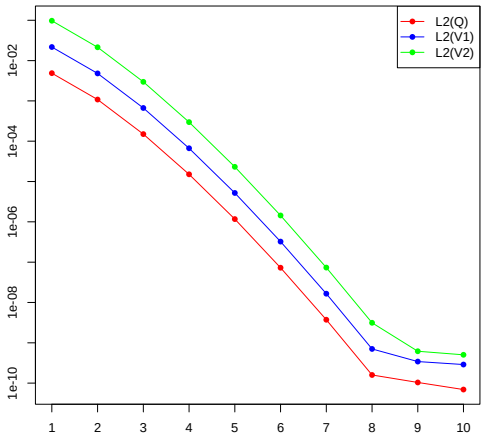

Figure 5. Proper orthogonal decomposition (POD) error in L2 norm. *x*-axis: number of modes, *y*-axis: error in L2 norm, in logarithmic coordinates.

With this development we can calculate the value of the lift for any value of the parameters, within the intervals that mark the CFD data. There is a huge computational advantage because we do not have to solve the CFD problem for those parameters. Instead we get an approximation with very few functions, which contain all the relevant information.

The computation time to calculate the lift-to-drag ratio value using the OpenFOAM CFD code for a set of parameters was approximately 52 min on a Workstation with 8 cores and 32 GB of RAM, while computing the approximation by POD took 2 s on a MacBook Pro with 3 GHz Intel Core i7. Another advantage of this method is that we can very easily design an algorithm that allows us to calculate the optimal parameters.

4. Results

4.1. Gurney Flaps

In order to determine the most advantageous size of the Gurney flap on the S810 aerodynamic airfoil a parametric study was carried. The first case investigated was the one without any GF implemented and the other twelve cases were with different sizes (y) of the GF, as illustrated in Table 1. Each case was studied for fifteen different angles of attack α, in the range from –4° to 10°. Figure 6 represents the evolution of the C_L/C_D ratio for each angle α and for every GF size. Figure 6a represents the lift-to-drag ratios for all GF cases against the airfoil angles of attack in comparison with the airfoil with no GF implemented. In the angle of attack (AoA) range from 0° to 6°, the best aerodynamic performance was achieved in the case with a GF size of 0.50% of c. In that range of AoAs, an increase on the lift-to-drag ratio around 70% in comparison with the clean case was achieved. From 6° to 10°, the GF size of 0.25% of c reached slightly better results than the case of 0.50% of c, but still very similar.

However, for negative AoAs from 0° to –4°, the highest lift-to-drag ratio was achieved by larger GF cases (around 2% of c). As illustrated in Figure 6b, the major values of C_L/C_D were achieved by GF sizes between 0.25% and 1% of c. This type of airfoil usually works with angles of attack between 4° and 6° at the nominal power. Therefore, the most promising GF size seems to be the one with 0.50% of c.

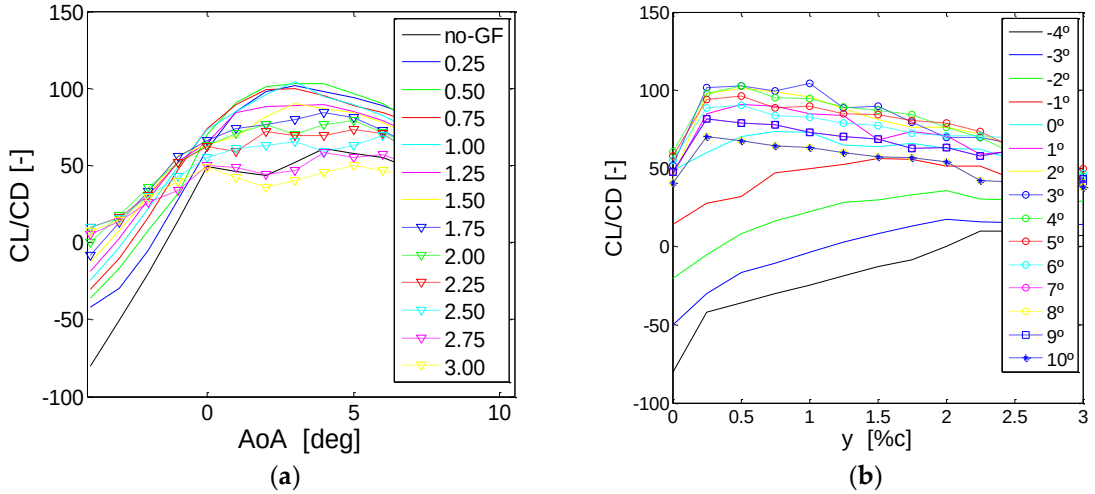

Figure 6. Lift-to-drag ratio C_L/C_D evolution for all GF cases: (**a**) for every angle of attack α and; (**b**) versus GF sizes.

Figure 7a,b represent the lift-to-drag ratio surfaces for the CFD and the POD results, respectively. The horizontals axes are the airfoil AoA in degrees and the length of the GF y in terms of percentage of the airfoil chord length. A 2D comparison between the CFD and the POD results is presented in Figure A1 of Appendix A for all cases. It is clearly visible that the CFD results were well-predicted by the POD approximation. Nevertheless, CFD data are required for reduced order method (ROM) calibration.

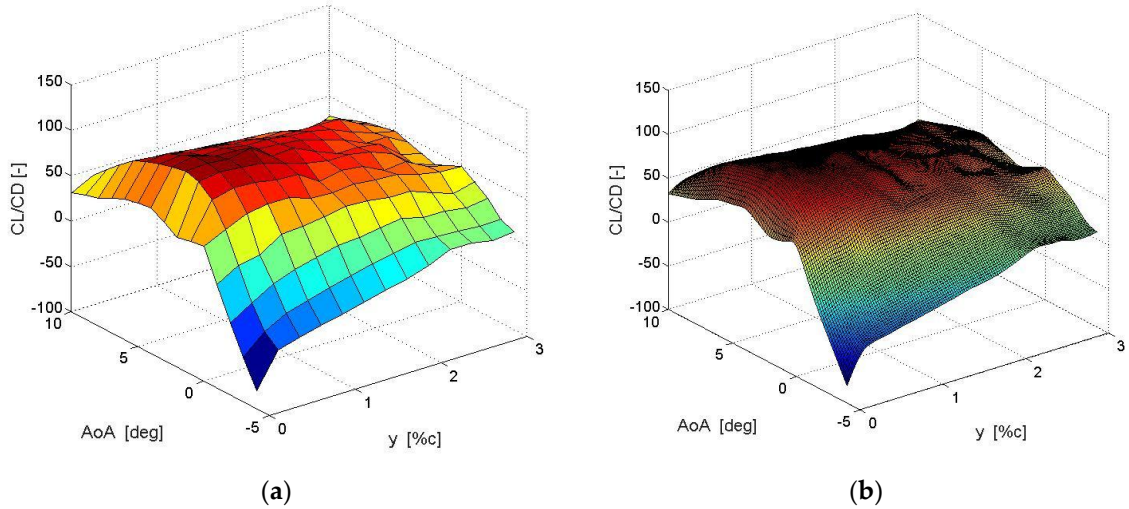

Figure 7. Lift-to-drag ratio surfaces. (**a**) CFD results and (**b**) recursive POD approximation results.

The results of the CFD and POD calculations for each AoA of the airfoil which achieved the maximum value of C_L/C_D are illustrated in Table 4. For both negative and positive angles of attack, the lift-to-drag ratios achieved by the POD method were similar to the results of the CFD method. Note that the POD approximation method was able to find the optimal GF size for each AoA in order to reach the maximum value of C_L/C_D.

Table 4. Results of the CFD and POD calculations for each AoA of the airfoil which achieved the maximum value of C_L/C_D with GFs.

AoA	CFD		POD	
	y (% c)	C_L/C_D [–] Max	y (% c)	C_L/C_D [–] Max
−4	2.50	10.01	2.3177	10.7903
−3	2.00	17.25	2.0569	17.5467
−2	2.00	36.01	1.9967	36.0020
−1	1.50	56.33	1.5753	56.3662
0	0.75	73.85	0.8528	74.1037
1	0.50	90.77	0.5117	90.7696
2	0.50	101.1	0.4415	101.4377
3	1.00	104.6	0.9732	104.9009
4	0.50	102.8	0.4615	103.1077
5	0.50	96.49	0.4314	97.1891
6	0.50	90.93	0.4314	90.9704
7	0.25	81.88	0.3010	82.3370
8	0.25	70.56	0.3110	71.1791
9	0.25	57.74	0.3512	58.3897
10	0.50	43.99	0.4314	44.1335

4.2. Microtabs

The optimal location of the MT on the airfoil DU91W(2)250 has been found by a parametric study following the cases presented in Table 3. Figure A2 of Appendix B represents the lift-to-drag ratios of all MT cases presented in Table 3 for each angle of attack. CFD results are presented in the left column, and the surface approximation generated by the POD method is in the right column.

The results of the CFD and POD calculations for each AoA of the airfoil DU91W(2)250 with and without MTs which achieved the maximum value of C_L/C_D are represented in Table 5. The lift-to-drag ratios estimated by the POD method were analogous to the results of the CFD method. Note that the POD approximation method was able to find the optimal MT size and position from the leading edge for each AoA in order to reach the maximum value of C_L/C_D. The best MT location from the leading edge was 95% of c, which agrees with the study of Fernandez-Gamiz et al. [26]. The most favorable MT size varied between 1% and 2% of the airfoil chord length. At low AoAs (between 0 and 5 degrees), the maximum lift-to-drag ratio was reached by the same case DU91W(2)250MT9520. However, as the AoA of the airfoil increased, the optimal value was achieved by smaller MTs with a size between 1% and 2% of c.

Table 5. Results of the CFD and POD calculations for each AoA of the airfoil which achieved the maximum value of C_L/C_D with MTs.

AoA	CFD			POD		
	x (% c)	y (% c)	C_L/C_D [–] Max	x (% c)	y (% c)	C_L/C_D [–] Max
0	95	2	82.37	95.02	2	82.54
1	95	2	102.5	95.03	2	102.6
2	95	2	122.2	95.03	2	122.2
3	95	2	141.6	95	2	141.6
4	95	2	160.8	95	2	160.8
5	95	2	179.9	95	2	179.9
6	95	1.5	189.5	95.03	1.306	199.1
7	95	1.5	80.48	95.06	1.345	80.77
8	95	1.5	85.23	95.06	1.229	85.45
9	95	1	78.61	95.03	1.224	80.66

According to the BEM-based computations of Fernandez-Gamiz et al. [26] and the wind turbine retrofitting study carried by Astolfi et al. [46], it is expected that the increase in the lift-to-drag ratio due to the implementation of passive flow control devices could lead to an increase in the wind turbine energy production. As explained in the work of Fernandez-Gamiz et al. [21] in a 5 MW wind turbine, the improvement in the power production could be more significant at low and moderate wind speeds. Additionally, the recursive POD developed in the current study could be easily implemented in the control system of a wind turbine to take advantage of active flow control strategies, which is in concordance with the study of Yen et al. [34], who presented MTs as devices with high potential for active load control.

5. Conclusions

Firstly, an investigation for the design and analysis of a GF on a S810 airfoil and of a MT on a DU91(2)250 airfoil was carried out. Two-dimensional computational fluid dynamic simulations were performed on these commonly used airfoils on wind turbines, using RANS equations at Re = 10^6. The GF and MT design attributes resulting from the CFD computations allowed sizing of the passive devices based on the airfoil aerodynamic performance. In both types of flow control devices, the results showed an increase in the lift-to-drag ratio for all angles of attack considered in the current work. In the case of the GFs, with AoAs from 0 to 6 degrees, the highest lift-to-drag ratio was achieved by the airfoil with the GF size of 0.50% of c. An enhancement of the lift-to-drag ratio around 70% in comparison with the clean case was achieved in that range of AoAs. From 6° to 10°, the GF size of 0.25% of c achieved superior but similar results to the case of 0.50% of c. It was found that the best MT location was 95% of c measured from the airfoil leading edge, and the most favorable MT size varied between 1% and 2% of the chord length of the airfoil. Between 0° and 6° of airfoil AoA, the maximum lift-to-drag ratio was reached by the case DU91W(2)250MT9515. Nevertheless, as the AoA of the airfoil increased beyond 6°, the most advantageous value was achieved by a shorter MT size.

Secondly, from the data obtained by means of CFD simulations, a regular function using the reduced order method of POD was built. In both flow control cases (GFs and MTs), the recursive POD method was able to accurately reproduce the computational results. The developed POD recursive method consists of two stages—one offline, and another online. The offline step consists of constructing the function that transforms the geometrical and physical parameters on the lift-to-drag ratio, starting from lift-to-drag ratio data obtained by CFD computations. In the online step, this function is used to directly compute the lift and drag coefficients for any given set of geometrical and physical parameters, without needing any CFD computation. This leads to a method with very low computational cost that is extraordinarily fast.

The results of the present work show that careful analysis of the GF size and MT height and location from the airfoil leading edge can yield effective devices for flow control in order to improve the airfoil aerodynamic performance. In addition, the POD method was revealed as a powerful tool to predict the lift-to-drag values of these types of parametric studies. The main conclusion of this paper is the validation of recursive POD approximation's ability to accurately compute the maximum lift–drag ratio associated with a given GF or MT configuration, in view of further applications in active flow control.

Author Contributions: Unai Fernandez-Gamiz prepared the case studies and performed the CFD simulations. Macarena Gomez-Mármol and Tomas Chacón Rebollo made the POD calculations. The manuscript was structured and written by all authors.

Funding: The current research was partially supported by the Spanish Government with the Project: grant number: MTM2015-64577-C2-1-R.

Acknowledgments: The authors are very grateful to the Spanish Government Project MTM2015-64577-C2-1-R.

Conflicts of Interest: The authors declare no conflict of interest.

Nomenclature

CFD	Computational Fluid Dynamics
BEM	Blade Element Momentum
GF	Gurney Flap
MT	Microtab
POD	Proper Orthogonal Decomposition
SVD	Singular Value Decomposition
PCA	Principal Components Analysis
ROM	Reduced Order Method
NREL	National Renewable Energy Laboratory
RANS	Reynolds Averaged Navier–Stokes
SST	Shear Stress Transport
PIV	Particle Image Velocimetry
AoA	Angle of Attack
Re	Reynolds number

Appendix A

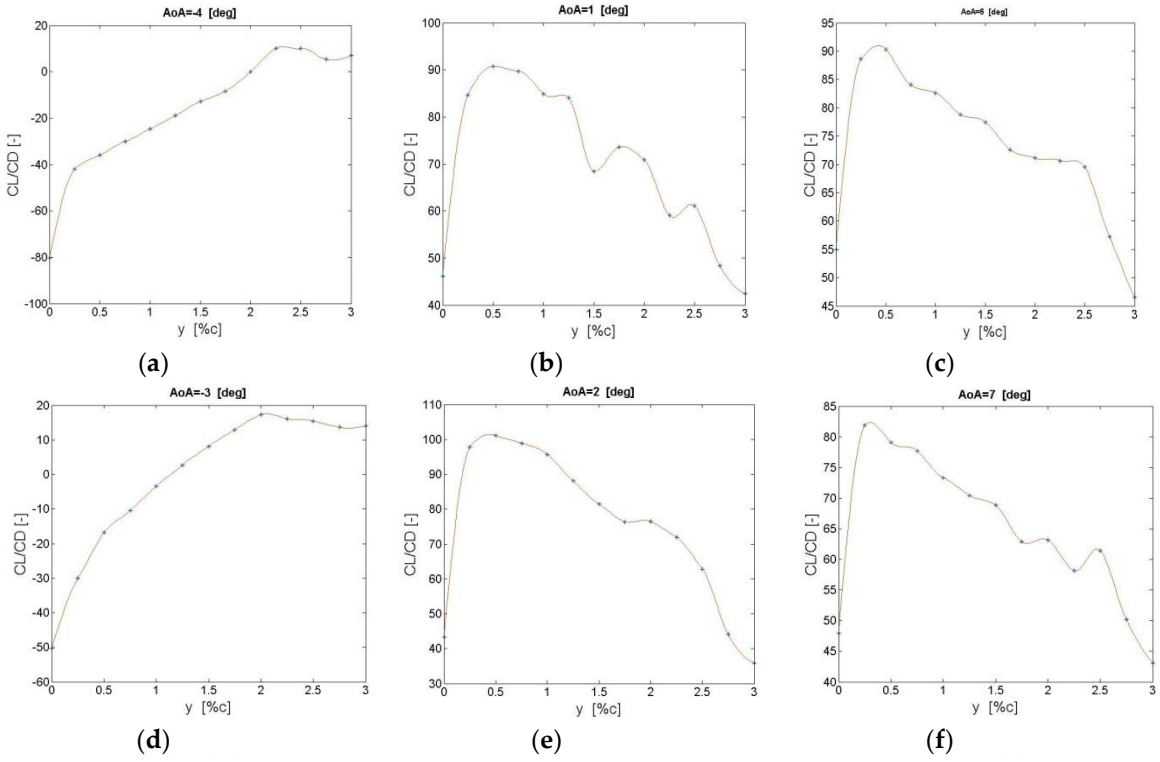

Figure A1. *Cont.*

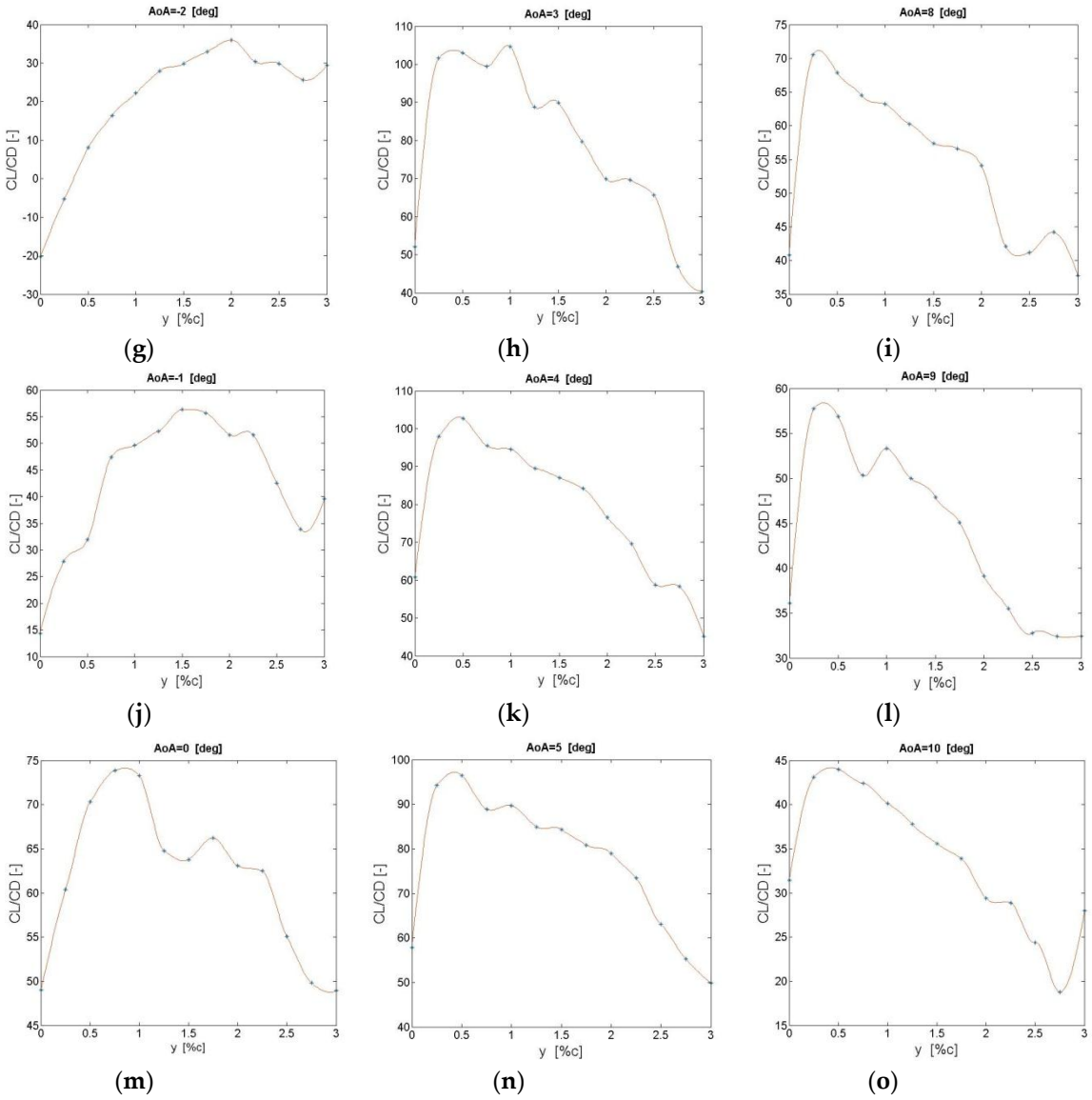

Figure A1. Lift-to-drag ratio of the S810 airfoil with GFs for each AoA. CFD results are denoted by * and the red line represents the POD approximation. Each sub-plot corresponds to an angle of attack AoA of the airfoil.

Appendix B

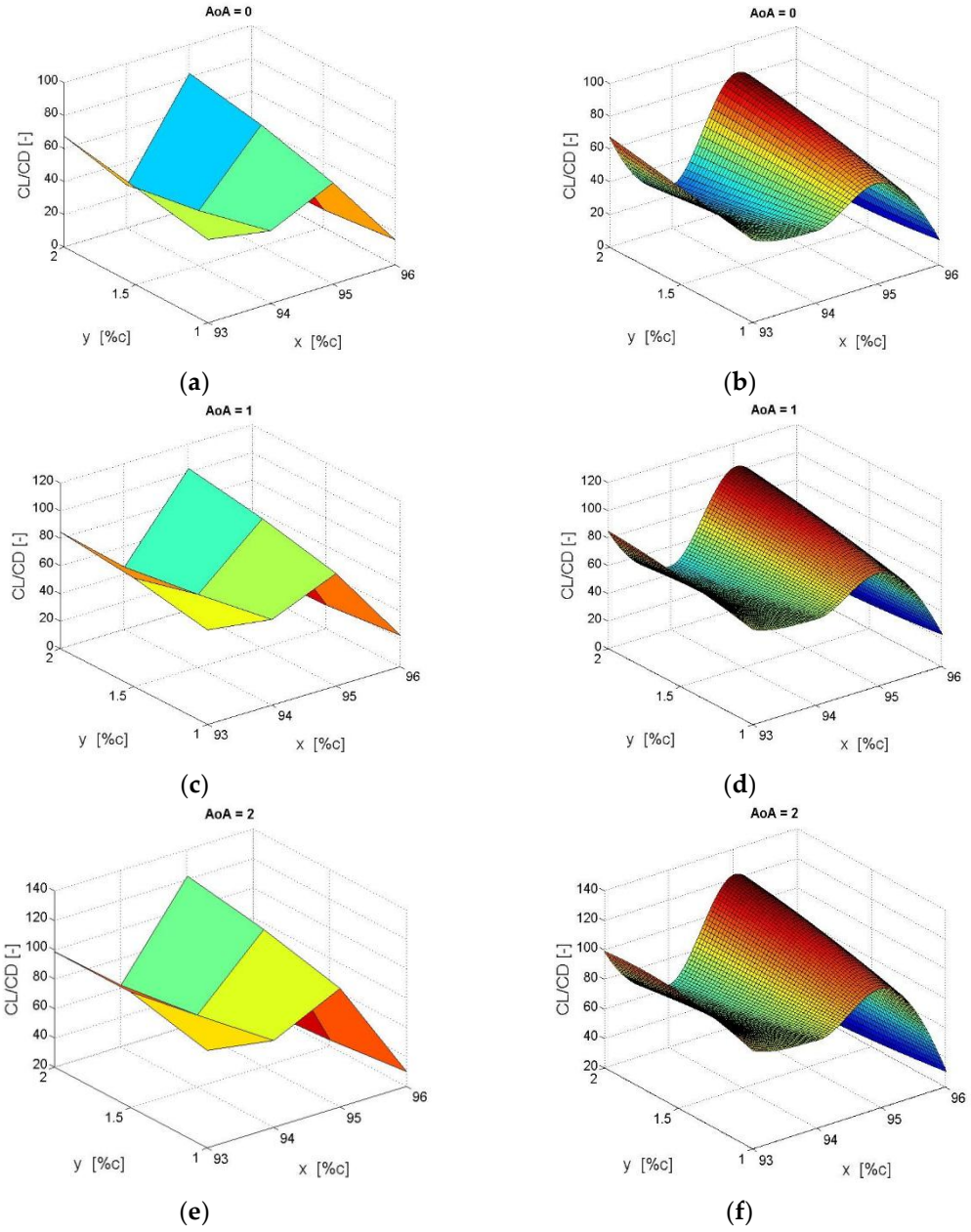

Figure A2. *Cont.*

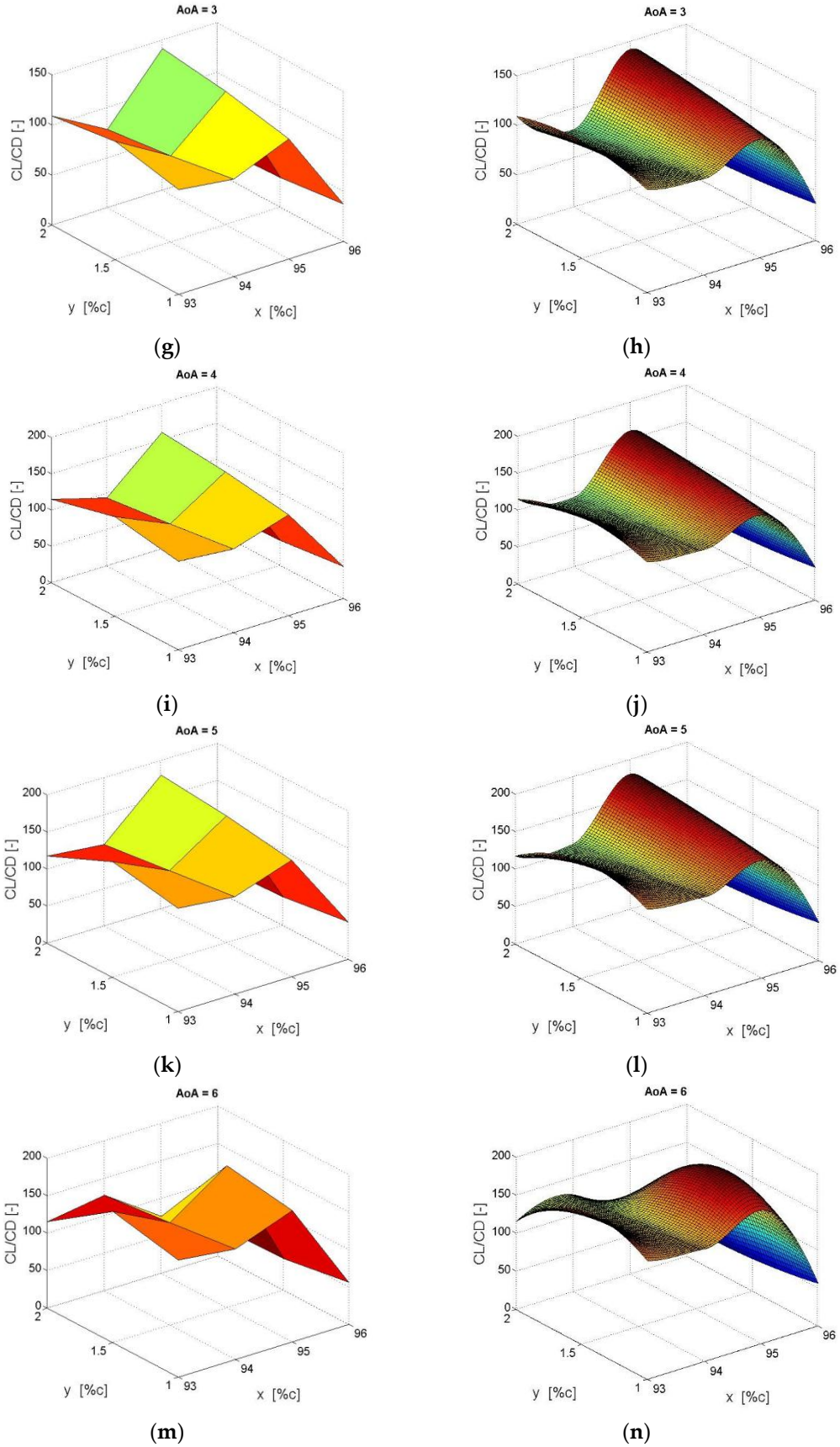

Figure A2. *Cont.*

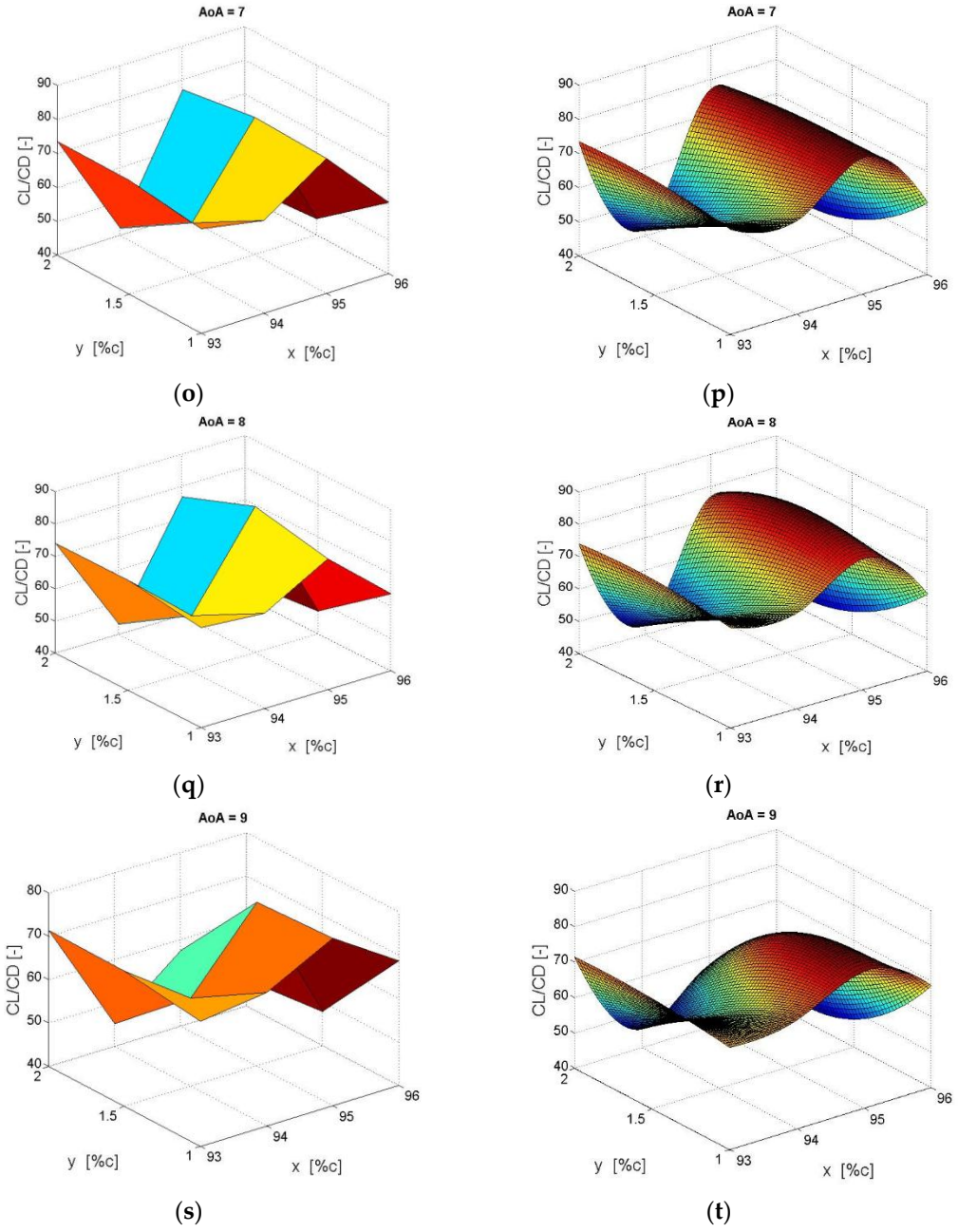

Figure A2. Lift-to-drag ratio of the DU91W(2)250 airfoil with MTs for each AoA. CFD results are represented in the left column and the POD approximation in the right one. Each sub-plot corresponds to an angle of attack AoA of the airfoil.

References

1. Johnson, S.J.; Dam, C.P. *Active Load Control Techniques for Wind Turbines*; Technical Report; Sandia National Laboratories: Livermore, CA, USA, August 2008.
2. Baek, P.; Gaunaa, M. Modeling the temporal response of a microtab in an aeroelastic model of a wind turbine. In Proceedings of the 49th AIAA Aerospace Sciences Meeting including the New Horizons Forum and Aerospace Exposition, Orlando, FL, USA, 4–7 January 2011.
3. Barlas, T.K.; Kuik, G.A.M. Review of state of the art in smart rotor control research for wind turbines. *Prog. Aerosp. Sci.* **2010**, *46*, 1–27. [CrossRef]

4. Wood, R.M. A Discussion of Aerodynamic Control Effectors Concepts (ACEs) for Future Unmanned Air Vehicles (UAVs). In Proceedings of the AIAA 1st Technical Conference and Workshop on Unmanned Aerospace Vehicle, Systems, Technologies, and Operations, Portsmouth, VA, USA, 20–23 May 2002.
5. Aramendia, I.; Fernandez-Gamiz, U.; Ramos-Hernanz, J.; Sancho, J.; Lopez-Guede, J.; Zulueta, E. Flow Control Devices for Wind Turbines. In *Energy Harvesting and Energy Efficiency: Technology, Methods, and Applications*; Bizon, N., Mahdavi Tabatabaei, N., Blaabjerg, F., Kurt, E., Eds.; Springer: Berlin, Germany, 2017; pp. 629–655.
6. Aramendia-Iradi, I.; Fernandez-Gamiz, U.; Sancho-Saiz, J.; Zulueta-Guerrero, E. State of the art of active and passive flow control devices for wind turbines. *Dyna* **2016**, *91*, 512–516. [CrossRef]
7. Johnson, S.J.; Baker, J.P.; van Dam, C.P.; Berg, D. An overview of active load control techniques for wind turbines with an emphasis on microtabs. *Wind Energy* **2010**, *13*, 239–253. [CrossRef]
8. Frederick, M.; Kerrigan, E.C.; Graham, J.M.R. Gust alleviation using rapidly deployed trailing-edge flaps. *J. Wind Eng. Ind. Aerodyn.* **2010**, *98*, 712–723. [CrossRef]
9. Woodgate, M.A.; Pastrikakis, V.A.; Barakos, G.N. Rotor computations with active gurney flaps. Presented at the ERCOFTAC Symposium on Unsteady Separation in Fluid-Structure Interaction, Mykonos, Greece, 17–21 June 2013; pp. 133–166.
10. Pastrikakis, V.A.; Steijl, R.; Barakos, G.N. Effect of active gurney flaps on overall helicopter flight envelope. *Aeronaut. J.* **2016**, *120*, 1230–1261. [CrossRef]
11. Wang, J.J.; Li, Y.C.; Choi, K.-S. Gurney flap-lift enhancement, mechanisms and applications. *Prog. Aerosp. Sci.* **2008**, *44*, 22–47. [CrossRef]
12. Liebeck, R.H. Design of Subsonic Airfoils for High Lift. *J. Aircr.* **1978**, *15*, 547–561. [CrossRef]
13. Jeffrey, D.; Zhang, X.; Hurst, D.W. Aerodynamics of gurney flaps on a single-element high-lift wing. *J. Aircr.* **2000**, *37*, 295–301. [CrossRef]
14. Lee, T.; Su, Y.Y. Lift enhancement and flow structure of airfoil with joint trailing-edge flap and gurney flap. *Exp. Fluids* **2010**, *50*, 1671–1684. [CrossRef]
15. Tang, D.; Dowell, E.H. Aerodynamic loading for an airfoil with an oscillating gurney flap. *J. Aircr.* **2007**, *44*, 1245–1257. [CrossRef]
16. Camocardi, M.; Marañon, J.; Delnero, J.; Colman, J. Experimental study of a naca 4412 airfoil with movable gurney flap. In Proceedings of the 49th AIAA Aerospace Sciences Meeting including the New Horizons Forum and Aerospace Exposition, Orlando, FL, USA, 4–7 January 2011.
17. Lee, T. Piv study of near-field tip vortex behind perforated gurney flaps. *Exp. Fluids* **2010**, *50*, 351–361. [CrossRef]
18. Cole, J.A.; Vieira, B.A.O.; Coder, J.G.; Premi, A.; Maughmer, M.D. Experimental Investigation into the Effect of Gurney Flaps on Various Airfoils. *J. Aircr.* **2013**, *50*, 1287–1294. [CrossRef]
19. Liu, L.; Padthe, A.K.; Friedmann, P.P. Computational study of microflaps with application to vibration reduction in helicopter rotors. *AIAA J.* **2011**, *49*, 1450–1465. [CrossRef]
20. Min, B.-Y.; Sankar, L.N.; Rajmohan, N.; Prasad, J.V.R. Computational Investigation of Gurney Flap Effects on Rotors in Forward Flight. *J. Aircr.* **2009**, *46*, 1957–1964. [CrossRef]
21. Fernandez-Gamiz, U.; Zulueta, E.; Boyano, A.; Ansoategui, I.; Uriarte, I. Five Megawatt Wind Turbine Power Output Improvements by Passive Flow Control Devices. *Energies* **2017**, *10*, 742. [CrossRef]
22. Chow, R.; Dam, C.P.V. Unsteady computational investigations of deploying load control microtabs. *J. Aircr.* **2006**, *43*, 1458–1469. [CrossRef]
23. van Dam, C.P.; Chow, R.; Zayas, J.R.; Berg, D.E. Computational investigations of small deploying tabs and flaps for aerodynamic load control. *J. Phys. Conf. Ser.* **2007**, *75*, 012027. [CrossRef]
24. Chow, R.; van Dam, C.P. On the temporal response of active load control devices. *Wind Energy* **2010**, *13*, 135–149. [CrossRef]
25. Tsai, K.-C.; Pan, C.-T.; Cooperman, A.; Johnson, S.; van Dam, C. An innovative design of a microtab deployment mechanism for active aerodynamic load control. *Energies* **2015**, *8*, 5885–5897. [CrossRef]
26. Fernandez-Gamiz, U.; Zulueta, E.; Boyano, A.; Ramos-Hernanz, A.J.; Lopez-Guede, M.J. Microtab Design and Implementation on a 5 MW Wind Turbine. *Appl. Sci.* **2017**, *7*, 536. [CrossRef]
27. Hwangbo, H.; Ding, Y.; Eisele, O.; Weinzierl, G.; Lang, U.; Pechlivanoglou, G. Quantifying the effect of vortex generator installation on wind power production: An academia-industry case study. *Renew. Energy* **2017**, *113*, 1589–1597. [CrossRef]

28. Lee, G.; Ding, Y.; Xie, L.; Genton, M.G. A kernel plus method for quantifying wind turbine performance upgrades. *Wind. Energy* **2014**, *18*, 1207–1219. [CrossRef]
29. Astolfi, D.; Castellani, F.; Terzi, L. Wind Turbine Power Curve Upgrades. *Energies* **2018**, *11*, 1300. [CrossRef]
30. Azaïez, M.; Belgacem, F.B.; Rebollo, T.C. Error bounds for POD expansions of parameterized transient temperatures. *Comput. Methods Appl. Mech. Eng.* **2016**, *305*, 501–511. [CrossRef]
31. Azaiez, M.; Ben Belgacem, F.; Chacón Rebollo, T. Recursive POD expansión for reaction-diffusion equation. *Adv. Mod. Simul. Eng. Sci.* **2016**, 3. [CrossRef]
32. Pinnau, R. Model Reduction via Proper Orthogonal Decomposition. In *Model Order Reduction: Theory, Research Aspects and Applications*; Springer: Berlin, Germany, 2008; pp. 95–109.
33. Chacon Rebollo, T.; Delgado Avila, E.; Gomez Marmol, M.; Ballarin, F.; Rozza, G. On a Certified Smagorinsky Reduced Basis Turbulence Model. *Siam J. Numer. Anal.* **2017**, *55*, 3047–3067. [CrossRef]
34. Yen, D.; van Dam, C.; Braeuchle, F.; Smith, R.; Collins, S. Active Load Control and Lift Enhancement Using MEM Translational Tabs. In Proceedings of the Fluids 2000 Conference and Exhibit, Denver, CO, USA, 19–22 June 2000. [CrossRef]
35. Ramsay, R.R.; Hoffmann, M.J.; Gregorek, G.M. *Effects of Grit Roughness and Pitch Oscillations on the S810 Airfoil*; Technical Report; National Renewable Energy Lab.: Golden, CO, USA, 1996; p. 152.
36. OpenFOAM. Available online: https://www.openfoam.org/ (accessed on 1 June 2017).
37. Menter, F. Zonal Two Equation k-w Turbulence Models for Aerodynamic Flows. In Proceedings of the 23rd Fluid Dynamics, Plasmadynamics, and Lasers Conference, Orlando, FL, USA, 6–9 July 1993. [CrossRef]
38. Kral, L.D. Recent experience with different turbulence models applied to the calculation of flow over aircraft components. *Prog. Aerosp. Sci.* **1998**, *34*, 481–541. [CrossRef]
39. Gatski, T.B. Turbulence Modeling for Aeronautical Flows. VKI Lecture Series: CFD-Based Aircraft Drag Prediction and Reduction. Available online: https://www.cfd-online.com/Forum/news.cgi/read/737 (accessed on 1 November 2003).
40. Mayda, E.A.; van Dam, C.P.; Nakafuji, D. Computational Investigation of Finite Width Microtabs for Aerodynamic Load Control. In Proceedings of the 43rd AIAA Aerospace Sciences Meeting and Exhibit, Reno, NV, USA, 10–13 January 2005. [CrossRef]
41. Thompson, J.F.; Warsi, Z.U.A.; Mastin, C.W. *Numerical Grid Generation*; Elsevier Science Publishing: London, UK, 1985.
42. Vinokur, M. On one-dimensional stretching functions for finite-difference calculations. *J. Comput. Phys.* **1983**, *50*, 215–234. [CrossRef]
43. Sørensen, N.N.; Mendez, B.; Munoz, A.; Sieros, G.; Jost, E.; Lutz, T.; Papadakis, G.; Voutsinas, S.; Barakos, G.N.; Colonia, S.; et al. CFD code comparison for 2D airfoil flows. *J. Phys. Conf. Ser.* **2016**, *753*. [CrossRef]
44. Timmer, W.A.; van Rooij, R.P.J.O.M. Summary of the Delft University wind turbine dedicated airfoils. *J. Sol. Energy Eng.* **2003**, *125*, 488–496. [CrossRef]
45. Jonkman, J.; Butterfield, S.; Musial, W.; Scott, G. *Definition of a 5 MW Reference Wind Turbine for Offshore System Development*; National Renewable Energy Laboratory: Golden, CO, USA, 2009.
46. Astolfi, D.; Castellani, F.; Terzi, L. A SCADA data mining method for precision assessment of performance enhancement from aerodynamic optimization of wind turbine blades. *J. Phys. Conf. Ser.* **2018**, *1037*. [CrossRef]